PROCEEDINGS OF SCIENCE

Challenges and Opportunities for Predicting Muons in Underground and Underwater Labs Using MUTE

William Woodley,[a,*] **Anatoli Fedynitch**[b] **and Marie-Cécile Piro**[a]

[a] *University of Alberta, Department of Physics*
4-181 CCIS, 116 St. and 85 Ave., Edmonton, AB T6G 2R3, Canada
[b] *Institute of Physics, Academia Sinica, Taipei City, 11529, Taiwan*
E-mail: wwoodley@ualberta.ca, anatoli@gate.sinica.edu.tw, mariecci@ualberta.ca

MUTE (MUon inTensity codE) is a Python program that combines two state-of-the-art codes, MCEQ and PROPOSAL, to predict muon intensities and spectra in underground and underwater laboratories. Our previous work [1] has demonstrated the accuracy of MUTE in reproducing the measured vertical equivalent muon intensities within the models' uncertainties. Moreover, we have shown that the experimental uncertainties are smaller than the theoretical uncertainties, making the vertical-equivalent data an effective calibration source for high-energy neutrino flux calculations. In this new study, we expand our analysis by calculating the total muon intensities and seasonal variations in labs located under flat earth and mountains using topographic maps of the overburdens. While our model predicts the amplitude of seasonal variations well, we identified inconsistencies amongst measurements at several labs, which pose additional challenges for interpretation. Additionally, the uncertainty in the rock density above many labs is a significant source of systematic uncertainty in total muon intensity measurements. Although MUTE accurately describes this data, we found that the uncertainties of the data were similar to our nominal prediction. We also present calculations using the DAEMONFLUX model, a muon and neutrino flux model calibrated with muon measurements at the surface, and using constraints from near-horizontal measurements at the highest energies. We examine whether the near-horizontal data is consistent with the underground measurements.

38th International Cosmic Ray Conference (ICRC2023)
26 July - 3 August, 2023
Nagoya, Japan

ICRC2023
38th International Cosmic Ray Conference
The Astroparticle Physics Conference

*Speaker

PoS(ICRC2023)476

1. Introduction

The unique opportunity to study high-energy muons without the technical challenges or costs associated with surface-based spectrometers, capable of resolving multi-hundred TeV range energies, is provided by large-volume detectors situated underground. In our previous work, we concentrated on the development of the MUTE code [1], a method designed for the efficient calculation of underground muon fluxes and other related observables. As a result, we deduced that a subset of underground muon measurements could serve as a "calibration source" for certain unconstrained model uncertainties, such as those recently incorporated by DAEMONFLUX [2]. In the present study, we scrutinise the residual body of related data using an updated version of MUTE. Our focus primarily lies on total muon fluxes and angular distributions as observed in laboratories situated beneath mountains, as well as on predictions of seasonal variations.

2. Computational Method

The computational scheme of MUTE (v1.0.1) used for labs under flat overburdens is described in [1]. In this follow-up work, we introduce MUTE v2 [3], capable of calculating muon observables for laboratories beneath mountains.[1] For the case of a flat overburden, symmetry in the azimuthal angle is assumed across all calculations, and there is a direct correspondence between slant depth, X, and zenith angle, θ, for a given vertical depth h:

$$X = \rho_{\text{rock}} \frac{h}{\cos(\theta)}, \tag{1}$$

where ρ_{rock} is the rock density. This relationship reduces the underground flux to a function of just two variables: underground energy, E^u, and zenith angle, $\Phi^u(E^u, \theta)$. For mountains, however, the shape of the mountain introduces dependence on the azimuthal angle to the amount of rock a muon has to travel through, meaning the geometry of the mountain has to be taken into account in the calculations. To do this, topographic maps of the mountains in terms of the depth $X(\theta, \phi)$ data are obtained from the labs (where ϕ is the azimuthal angle), such as the one for LNGS shown in Figure 1. For this reason, slant depth and zenith angle are kept as separate variables in the calculation of underground fluxes: $\Phi^u(E^u, X(\theta, \phi), \theta)$.

For both overburden types, the differential muon intensity is given by integrating the underground flux over the underground energy:

$$I^u(\theta, \phi) = \int_{E_{\text{th}}}^{\infty} \Phi^u(E^u, X(\theta, \phi), \theta)\, \mathrm{d}E^u, \tag{2}$$

where E_{th} is a choice for the threshold energy. We implement the calculation of the double-differential intensity in MUTE v2, by precomputing an underground intensity $I^u(X, \theta)$ on a constant grid of depths X and zenith angles θ. We then interpolate this distribution for a specific overburden profile $X(\theta, \phi)$, where we again assume azimuthal symmetry for muon fluxes at the surface. From this, we obtain a matrix of intensities $I^u(\theta, \phi)$, corresponding to the binning of the numerical representation of the mountain maps $X(\theta, \phi)$ provided directly by the experimental collaborations.

[1] https://github.com/wjwoodley/mute

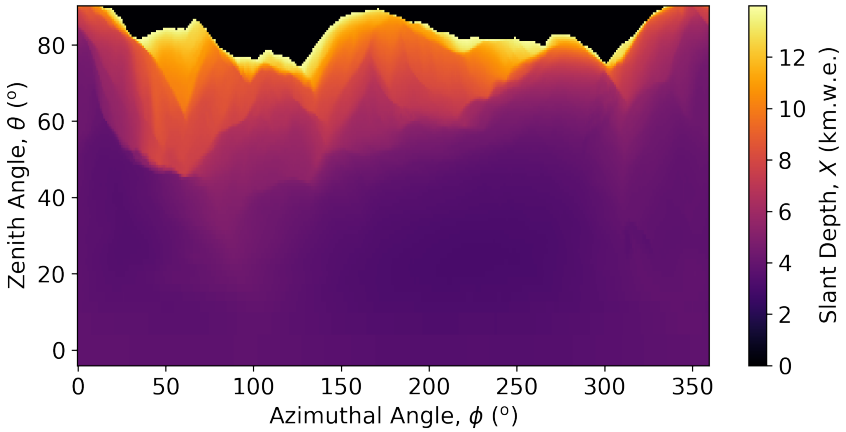

Figure 1: A plot of the slant depths of the Gran Sasso mountain, $X(\theta, \phi)$, in terms of zenith and azimuthal angle. Depths greater than 14 km.w.e. have been masked (shown in black), as 14 km.w.e. is the default maximum slant depth for which calculations can be done by MUTE.

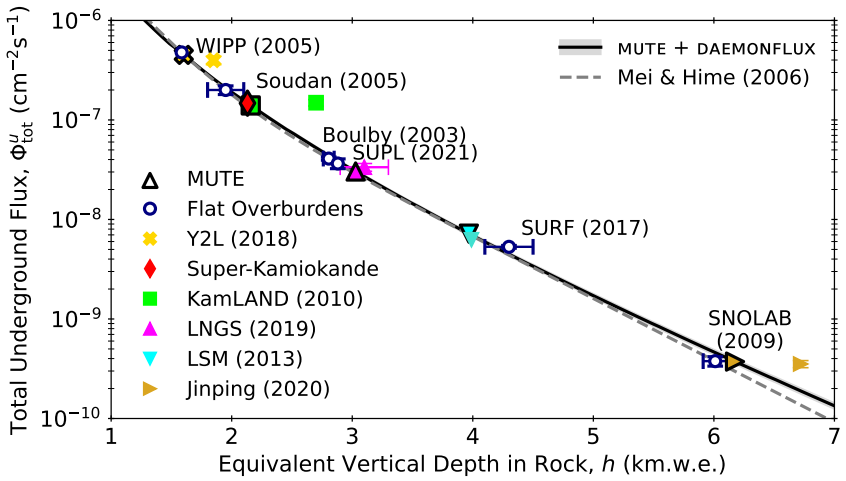

Figure 2: Total underground muon flux vs equivalent vertical depth underground. The MUTE curve was calculated for a flat overburden, and the points with thick black outlines were calculated using MUTE with mountain maps. The latter have had their depth values fitted to lie on the DAEMONFLUX curve, giving the laboratory's equivalent vertical depth. Experimental data is shown for WIPP [4], Y2L [5], Soudan [6], KamLAND [7], Boulby [8], SUPL [9], LNGS [10], LSM [11], SURF [12], SNOLAB [13], and Jinping [14]. For comparison, the curve from the parametric formula from [15] is also shown.

Using this scheme, we can calculate two-dimensional maps of muon intensities and the total (angle-integrated) muon fluxes that can be compared with data from underground and underwater detectors.

3. Total Muon Flux

The total underground muon flux is the main physical observable of interest for muon-induced backgrounds in direct Dark Matter (DM) detectors. It is calculated by integrating the underground

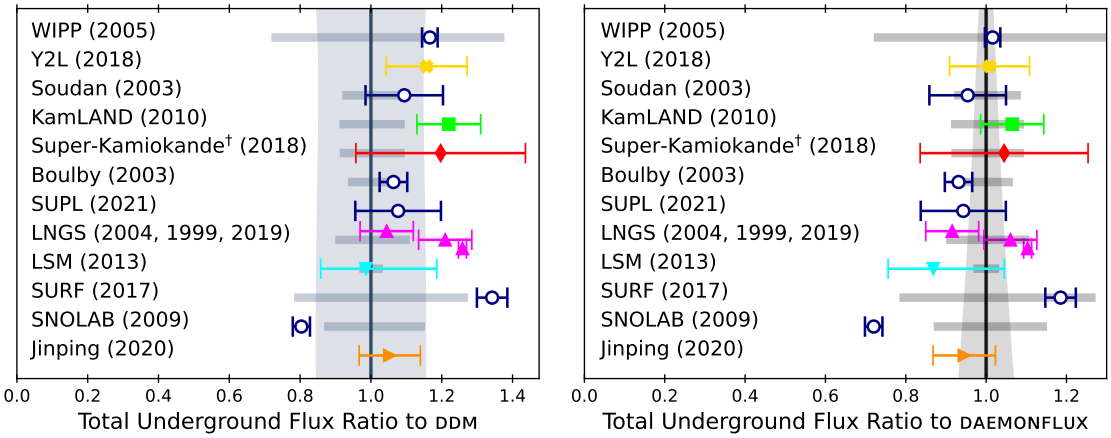

Figure 3: The ratio of experimental total underground muon flux measurements to MUTE using DDM (left) DAEMONFLUX (right). The error band represents the uncertainty in the hadronic interaction model from DDM, while the horizontal bars represent uncertainty in the rock density. Experimental data is cited in Figure 2 with the addition of Super-Kamiokande here [16]. A dagger (†) indicates that the point used is a prediction calculated from simulation and does not come from experimental data.

intensity from Equation 2 over the solid angle:

$$\Phi^{\mu} = \iint_{\Omega} I^{\mu}(X(\theta,\phi),\theta)\,\mathrm{d}\Omega. \tag{3}$$

This calculation has been done for various sites under rock using DAEMONFLUX as the surface muon flux model. The results are shown in Figure 2, with a curve calculated for flat overburdens as a reference from which the equivalent vertical depths for labs are defined. Note that an equivalent vertical depth for labs beneath mountains is an inferred quantity derived from comparing the observed (or predicted) muon flux with the equivalent flux level under a flat overburden. Values calculated using MUTE are shown with thick black outlines and those without outlines (with the same colours and shapes) are experimental measurements. Some of the official data points shown in Figure 2 are offset with respect to the MUTE result along the x-axis. This is due to the experiments reporting those at an "engineering depth" instead of a vertical equivalent depth defined through muon observations.

The ratio of the observed to the predicted total muon fluxes is shown in Figure 3, along with the model uncertainty estimation from DDM [17] (left) and DAEMONFLUX (right). The horizontal blue and grey bars show the systematic uncertainty of the predictions due to the limited knowledge of the overburden density. We observe almost no systematic shift with respect to the total flux data with the DAEMONFLUX model, whereas the MUTE v1 baseline, DDM, has noticeably larger errors and appears systematically lower than data. MUTE in combination with DAEMONFLUX provides a satisfactory description of the data within the uncertainties of the data. A notable exception is SNOLAB [13], where the data cannot be described by the model.

Total muon flux measurements in water can be performed by water Cherenkov detectors, such as the KM3NeT detectors [19]. The comparison between MUTE, a typical reference calculation [18], and an early KM3NeT measurement is shown in Figure 4. The only change in the MUTE calculation

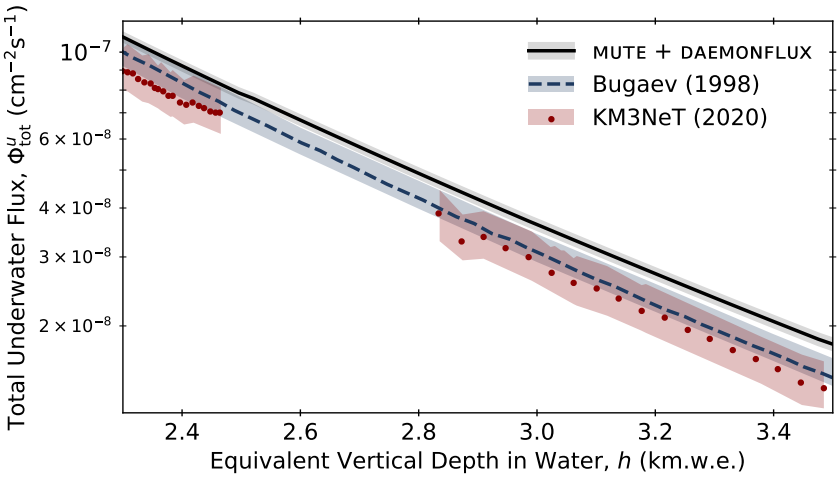

Figure 4: Total muon flux vs slant depth in fresh water. The curve for DAEMONFLUX was calculated using MUTE with a flat overburden. A curve is also included for the theoretical calculation of Bugaev, et al. [18]. KM3NeT data is taken from [19].

is from standard rock to water in the PROPOSAL code used for transfer tensor generation. Hence, the precision seen in rock should be applicable to water as well. We note that KM3NeT's data is a factor of 2 below the prediction. We look forward to comparing to results from a more complete version of the detectors and analysis pipelines.

4. Seasonal Variations

A long-known feature of the atmospheric muon flux is its variation over the seasons [20, 21]. This is primarily caused by the change in temperature of the stratosphere between summer and winter, and the result is driven by the two competing options for pions and kaons to either interact or decay. As the atmosphere warms, it becomes less dense and the altitude of the production level of pions and kaons increases. When the atmosphere is less dense, pions and kaons undergo fewer interactions and so are more likely to interact instead of decay into muons. However, this process is energy-dependent [22]. The consequence is that we expect different seasonal variations at the surface and underground, since the mean muon energies seen by detectors at the surface are in the GeV range, whereas they are in the TeV range underground.

Figure 5 is calculated using muon fluxes computed with MCEQ [22], using the SIBYLL-2.3C interaction model [29] and the NRLMSISE-00 model of the Earth's atmosphere [30]. The amplitude of seasonal variations is defined as

$$A = \text{sign}\left(\Phi^{\mu}_{\text{tot, Jul.}} - \Phi^{\mu}_{\text{tot, Jan.}}\right)\left(\frac{\Phi^{\mu}_{\text{tot, max}} - \Phi^{\mu}_{\text{tot, min}}}{2\left\langle\Phi^{\mu}_{\text{tot}}\right\rangle}\right), \tag{4}$$

and depends substantially on latitude. Seasonal variations at the surface and at 3 km.w.e. underground are opposite in sign to each other, and the most extreme variations occur underground at the poles.

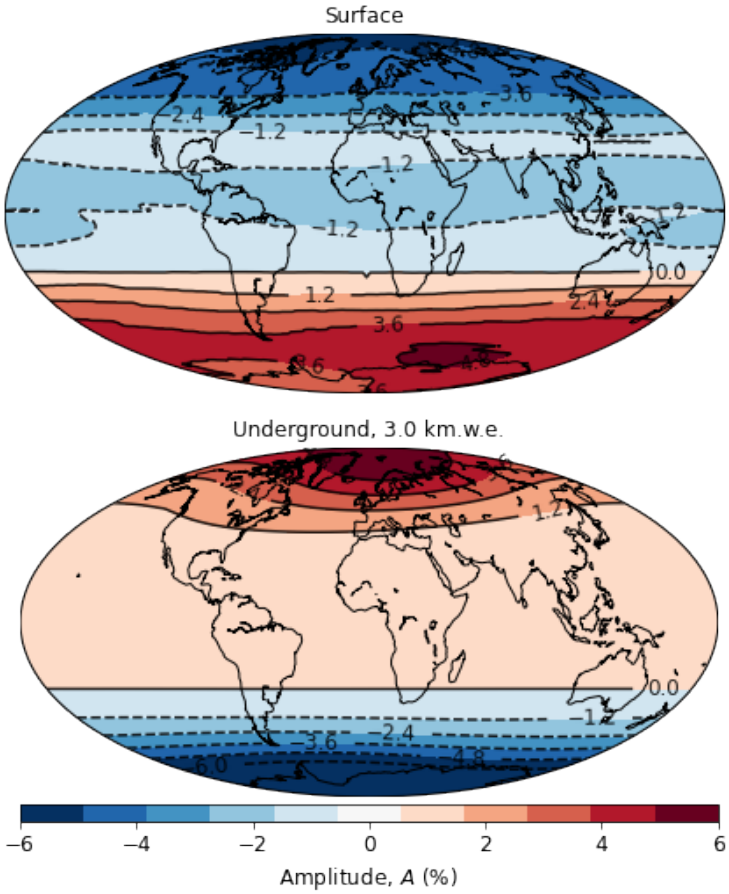

Figure 5: Maps ($2^\circ \times 2^\circ$) of amplitudes of the seasonal variation in the muon flux at the surface of the Earth (top) and 3 km.w.e. underground (bottom). Positive amplitude (red) indicates the flux peaks around July, and negative amplitude (blue) indicates the flux peaks around January.

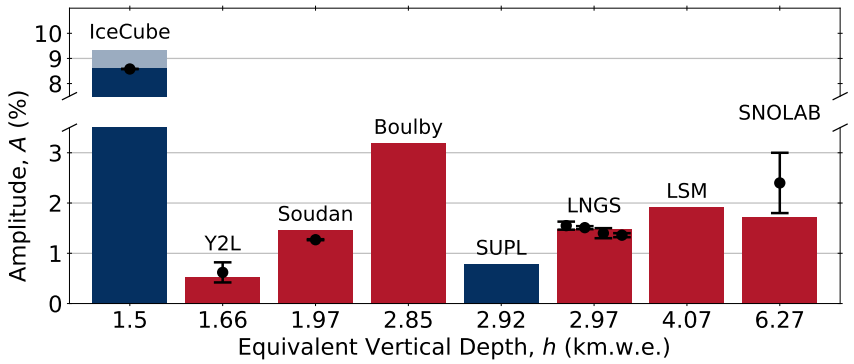

Figure 6: Amplitude of seasonal variations in the underground muon flux for select laboratories. Red is used for labs in the northern hemisphere, with a peak in the muon flux in July, and blue is used for labs in the southern hemisphere, with a peak in January, comparable to Figure 5. For IceCube, the darker blue bar indicates the amplitude at the top of the instrumented volume (~ 1.5 km.w.e.), whereas the lighter bar is for the bottom (~ 2.5 km.w.e.). Experimental measurements are shown by black points for IceCube [23], Y2L [24], Soudan [25], LNGS [10, 21, 26, 27], and SNOLAB [28].

The amplitudes at select laboratories are shown in Figure 6 with experimental data added where available. Because the IceCube detector is located at the South Pole it observes the most extreme muon and neutrino seasonal variations on the planet [23, 31].

5. Conclusion

Our study introduces MUTE v2, an improved tool for calculating muon fluxes in underground and underwater laboratories, designed to account for complex geographical features such as mountainous terrain. Our model matches observed data for most locations within the uncertainties, demonstrating its robustness and utility in predicting underground muon fluxes, particularly relevant for cosmic ray and DM detection. We observed discrepancies at SNOLAB, suggesting that careful evaluation of data is required for obtaining additional flux model constraints as in DAEMONFLUX.

While MUTE's precision can be evaluated using a larger set of data from underground laboratories, it can be applied to underwater environments without significant loss of predictive power. We found a discrepancy between early KM3NeT data and our model predictions, and we await more extensive data sets for further analysis.

We also explored the seasonal variations in the underground muon flux, noting the distinct variation patterns at surface level versus those deep underground, influenced by geographical and energy-dependent factors. We observed good compatibility with available data.

Overall, MUTE v2 provides a robust basis for exploring underground muon flux data for indirect studies of muon and neutrino flux uncertainties in the TeV to PeV range at the surface. Due to a rigorously derived error estimate, MUTE may find unique applications in the characterisation of muon-induced backgrounds for DM searches and other low-background underground experiments.

Acknowledgements

We acknowledge the help of Marco Selvi and the LVD collaboration, who provided us with the data for the muon angular distribution and the topographic map of the Gran Sasso mountain. We acknowledge, as well, the help of Michel Zampaolo and Luigi Mosca for the data of the Fréjus detector, and Holger Kluck and Wolfgang Rhode for a map of the Fréjus mountain. We also acknowledge Eunju Jeon and Hyun Su Lee, who provided us with a topographic map of the Yangyang mountain, Itaru Shimizu and Shigetaka Moriyama for the maps of the Kamioka mountain, and Shaomin Chen for the map of the Jinping mountain from JNE data. This research was enabled in part by support provided by the Digital Research Alliance of Canada. W. Woodley and M.-C. Piro acknowledge the support from the Canada First Research Excellence Fund through the Arthur B. McDonald Canadian Astroparticle Physics Research Institute.

References

[1] A. Fedynitch, W. Woodley and M.-C. Piro, *Astrophys. J.* **928** (2022) 27 [2109.11559].

[2] J.P. Yañez and A. Fedynitch, 2303.00022.

[3] W. Woodley and A. Fedynitch, July, 2022. 10.5281/zenodo.6841971.

[4] E.-I. Esch, T.J. Bowles, A. Hime, A. Pichlmaier, R. Reifarth and H. Wollnik, *Nucl. Instrum. Meth. A* **538** (2005) 516 [astro-ph/0408486].

[5] COSINE-100, *PoS* **ICRC2017** (2018) 883.

[6] S. Kamat, Ph.D. thesis, Case Western Reserve U., 2005. 10.2172/15017230.

[7] KamLAND, *Phys. Rev. C* **81** (2010) 025807 [0907.0066].

[8] M. Robinson, V.A. Kudryavtsev, R. Luscher, J.E. McMillan, P.K. Lightfoot, N.J.C. Spooner et al., *Nucl. Instrum. Meth. A* **511** (2003) 347 [hep-ex/0306014].

[9] W.D. Melbourne, *J. Phys. Conf. Ser.* **2156** (2021) 012064.

[10] LVD, *Phys. Rev. D* **100** (2019) 062002 [1909.04579].

[11] EDELWEISS, *Astropart. Phys.* **44** (2013) 28 [1302.7112].

[12] MAJORANA, *Astropart. Phys.* **93** (2017) 70 [1602.07742].

[13] SNO, *Phys. Rev. D* **80** (2009) 012001 [0902.2776].

[14] JNE, *Chin. Phys. C* **45** (2021) 025001 [2007.15925].

[15] D. Mei and A. Hime, *Phys. Rev. D* **73** (2006) 053004 [astro-ph/0512125].

[16] Hyper-Kamiokande, 1805.04163.

[17] A. Fedynitch and M. Huber, *Phys. Rev. D* **106** (2022) 083018 [2205.14766].

[18] E.V. Bugaev, A. Misaki, V.A. Naumov, T.S. Sinegovskaya, S.I. Sinegovsky and N. Takahashi, *Phys. Rev. D* **58** (1998) 054001 [hep-ph/9803488].

[19] KM3NeT, *Eur. Phys. J. C* **80** (2020) 99 [1906.02704].

[20] P.H. Barrett, L.M. Bollinger, G. Cocconi, Y. Eisenberg and K. Greisen, *Rev. Mod. Phys.* **24** (1952) 133.

[21] Borexino, *JCAP* **02** (2019) 046 [1808.04207].

[22] A. Fedynitch, R. Engel, T.K. Gaisser, F. Riehn and T. Stanev, *EPJ Web Conf.* **99** (2015) 08001 [1503.00544].

[23] IceCube, *PoS* **ICRC2019** (2020) 894 [1909.01406].

[24] COSINE-100, *JCAP* **02** (2021) 013 [2005.13672].

[25] MINOS, *Phys. Rev. D* **91** (2015) 112006 [1503.09104].

[26] OPERA, *JCAP* **10** (2019) 003 [1810.10783].

[27] GERDA, *Astropart. Phys.* **84** (2016) 29 [1601.06007].

[28] C.C.M. Kyba, Ph.D. thesis, University of Pennsylvania, 2006.

[29] A. Fedynitch, F. Riehn, R. Engel, T.K. Gaisser and T. Stanev, *Phys. Rev. D* **100** (2019) 103018 [1806.04140].

[30] J.M. Picone, A.E. Hedin, D.P. Drob and A.C. Aikin, *Journal of Geophysical Research: Space Physics (1978–2012)* **107** (2002) SIA 15.

[31] R. Abbasi et al., 2303.04682.